Effects of phase ratios, density and particle shapes on directional thermal conductivity of vegetable concrete: A predictive model

Nils Frantz, Lorena Freitas Dutra, Dang Mao Nguyen, Giana Almeida, Patrick Perré

To cite this version:

Nils Frantz, Lorena Freitas Dutra, Dang Mao Nguyen, Giana Almeida, Patrick Perré. Effects of phase ratios, density and particle shapes on directional thermal conductivity of vegetable concrete: A predictive model. Construction and Building Materials, 2024, 410, pp.134238. ⟨10.1016/j.conbuildmat.2023.134238⟩. ⟨hal-04303463⟩

HAL Id: hal-04303463
https://hal.science/hal-04303463v1

Submitted on 15 Jul 2024

Effects of phase ratios, density and particle shapes on directional thermal conductivity of vegetable concrete: a predictive model

Nils Frantz[a], Lorena Freitas Dutra[b], Dang Mao Nguyen[c], Giana Almeida[d], Patrick Perré[a,e,*]

[a] *Université Paris-Saclay, CentraleSupélec, LGPM, Centre Européen de Biotechnologie et de Bioéconomie (CEBB), 3 rue des Rouges Terres, 51 110 Pomacle, France*
[b] *Université de Picardie Jules Verne, LTI, Avenue des Facultés - Le Bailly, 80 025 Amiens, France*
[c] *Ecole Supérieure du Bois (ESB), LIMBHA, Rue Christian Pauc, 44306 Nantes, France*
[d] *Université Paris-Saclay, INRAE, AgroParisTech - UMR SayFood - 22 place de l'Agronomie, 91 120 Palaiseau, France*
[e] *Université Paris-Saclay, CentraleSupélec, LGPM, 3 rue Joliot Curie, 91 190, Gif-sur-Yvette, France*

Abstract

This work is devoted to the thermal conductivity of vegetable concrete (Lime-hemp concrete). Various parameters were investigated using a design of experiment : 5 categories of particle size, 3 binder/particle ratios (1, 1.5 and 2) and 3 target densities (300, 400 and 500 $kg.m^{-3}$). The thermal conductivity was measured in steady-state across and along particles. The results clearly depict the effect of direction on thermal conductivity, but prove that density alone is not a good predictor. As an innovative outcome, the porosity was proved to be a good indicator of the respective weights of the parallel and serial conductivity. This is explained by the negative effect of porosity on the connectivity of the binder, which was confirmed by CT scans. The effect of particle size distribution remains weak, except for the category *Small*, which has also the lowest elongation and for which the conductivity is nearly isotropic. General expressions are proposed to predict the conductivity from the characteristics of vegetable concretes (proportions, densities and conductivities of the gas, particle and binder phases).

Keywords: anisotropy, hemp, lime, porosity, porous medium

Highlights

- Lime-hemp concretes with various parameters manufactured using a design of experiment

---

[*] Corresponding author
Email address: `patrick.perre@centralesupelec.fr` (Patrick Perré)

- The measured conductivity depends on direction but is poorly explained by density
- Porosity proposed as predictor of the proportion between series and parallel models
- The directional conductivities are accurately predicted from manufacturing parameters
- The effect of particle size distribution is mostly explained by the particle elongation

CRediT author statement

NF: Investigation, Methodology, Visualization, Writing-Original draft preparation. LFD: Investigation, Methodology, Supervision, Writing-Reviewing and Editing. MN: Supervision, Writing-Reviewing and Editing. GA: Investigation, Methodology, Visualization, Supervision, Writing-Reviewing and Editing. PP: Conceptualization, Methodology, Formal analysis, Software, Visualization, Supervision, Writing-Original draft preparation, Writing-Reviewing and Editing, Project administration, Funding acquisition.

Graphical abstract

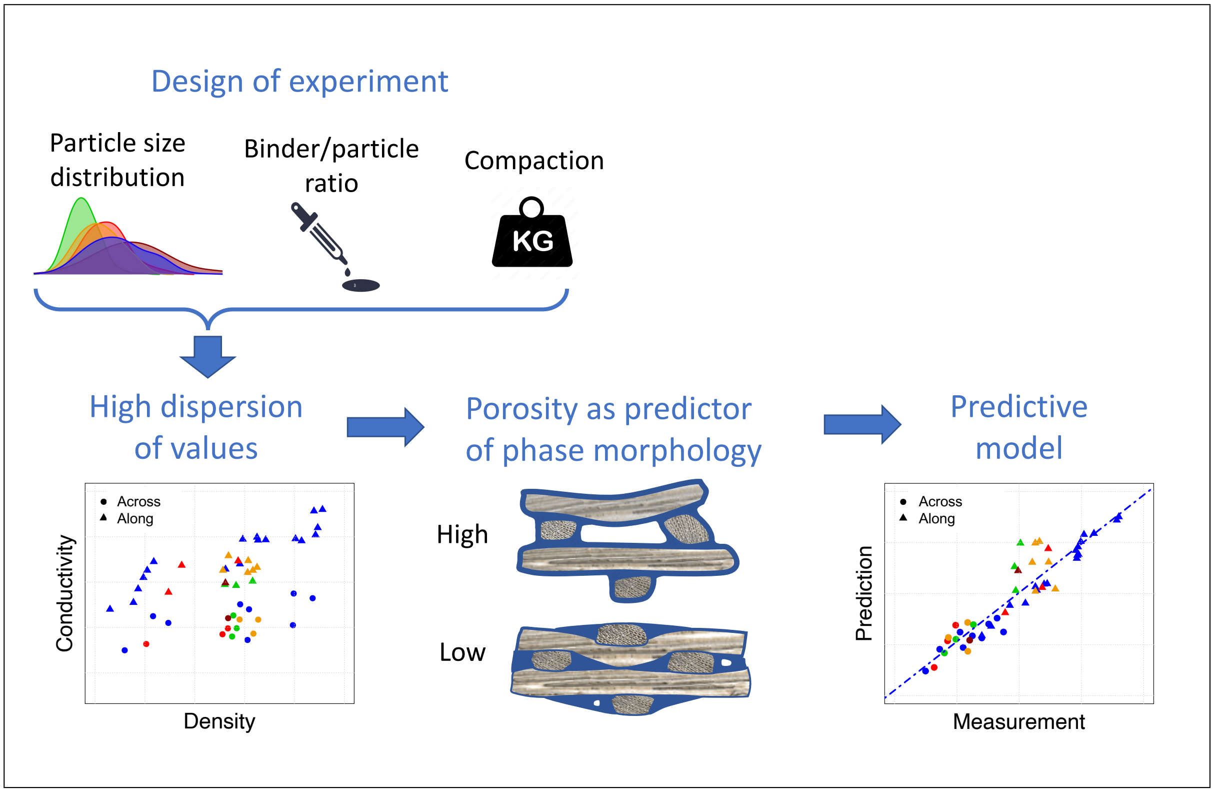

1. Introduction

Bio-based materials play an important role in the energy and ecological transitions thanks to their ability to store carbon and their low embodied energy. One third of the 27% of global greenhouse gas emissions from the building sector would be attributable to construction materials (IEA, 2021). In fact, this sector is responsible for more than a third of the world's consumption of abiotic resources (UN environnement, 2016). Although the performance of biobased materials is not easy to predict, they are likely to perform all the functions required of a building's external wall, including the required compromise between the structural and thermal insulation aspects of the envelope.

Among them, Lime-Hemp Concrete (LHC) is of great interest in the field of construction because of its low environmental impact (Florentin et al., 2017), its good mechanical resistance (Walker et al., 2014) and outstanding hygro-thermal properties, notably due to the low density of hemp shives (Arnaud and Gourlay, 2012; Page et al., 2017). Due to its good compromise between different functions, it is therefore used as a bio-sourced material for buildings (Collet et al., 2013; Walker and Pavía, 2014; Oumeziane et al., 2016; Benmahiddine et al., 2020). In particular, an improvement in the combination of thermal insulation and compressive strength would enable LHC to be used as a single wall for the construction of buildings with low environmental impact (Sáez-Pérez et al., 2020). The thermal inertia provided by this material would improve the resistance of homes to global warming regarding summer comfort (Shea et al., 2012; Gourlay et al., 2017; Costantine et al., 2020; Bennai et al., 2022). The identification of the best configurations therefore requires a better understanding of the factors influencing wall thermal conductivity.

This study focuses on the link between the LHC characteristics and thermal conductivity. This conductivity has been reported to vary in the range 0.06 to 0.16 $W.m^{-1}.K^{-1}$ at room temperature (Hajmohammadian Baghban et al., 2013; Walker and Pavía, 2014; Haik et al., 2020; Gündüz and Şahin, 2021; Brzyski et al., 2021). This wide range is due to the effect of various parameters such as temperature, moisture content and density (Collet et al., 2013; Collet and Prétot, 2014; Pierre et al., 2014; Seng et al., 2019; Asli et al., 2021). Linear correlations were proposed to better predict thermal conductivity of LHC from these parameters, with a main focus on density (Cerezo, 2005; Collet and Prétot, 2014; Real et al., 2016; Gourlay et al., 2017). In addition to density, other studies investigated the influence of the anisotropic morphology of these materials on thermal conductivity (Nguyen, 2010; Magniont et al., 2012; Pierre et al., 2014; Tran-Le et al., 2019; Seng et al., 2019). They indicated that the hemp shives are oriented during manufacturing, which makes the thermal conductivity higher in the direction orthogonal to compaction (Williams et al., 2016, 2018; Brzyski et al., 2021).

Besides experimental measurements, modeling approaches able to predict the thermal property trends are interesting tools to recommend manufacturing rules or to save time and cost of characterization. Several models have been developed for LHC. For example a theoretical model (Boutin, 1996) and a multi-scale homogenization approach which allows to study of the effect of shape/orientation of particles and pore on the effective thermal conductivity tensor (Nguyen et al., 2016; Dartois et al., 2017; Tran-Le et al., 2019; Huang et al., 2023). However, these predictive tools need the full description of the morphology, which is a complex challenge. The literature review shows that there is not yet an operational model that can effectively predict thermal conductivity by fully taking into account the influence of various parameters such as binder/particle mass ratio (B/P), density, porosity and anisotropy.

The aim of this paper is to study the thermal conductivity of LHC for a large database of various material realizations. A considerable amount of experimental work has been carried out, based on a design of experiment, to produce LHC with controlled factors (B/P ratio, density, porosity, size of hemp shives). The thermal conductivity of these materials was measured experimentally across and along the compaction direction. This database allowed an original analytical model to be derived using the material porosity as synthetic indicator. Based on this approach, expressions are proposed to predict the directional thermal conductivities of lime-hemp concrete as a function of the manufacturing parameters.

2. Materials and methods

The hemp shives used for the production of concrete were provided by Agrochanvre (Normandy, France). The hemp particles used in the study come from the same batch, harvested in September 2021. Indeed, some studies have highlighted the influence of the plant environment (climate, soil) during growth and retting on the chemical composition and extractives content of hemp shives (Liu et al., 2015; Hajj Obeid et al., 2022). These effects are therefore discarded in this study. The shives were stored at room conditions until the preparation of the particles. The formulated binder used for the manufacturing concrete is Tradical® Thermo binder, composing of about 80% hydraulic lime and 20% cement. The Methyl Cellulose used as additive was supplied by DEFI - Houillères de Cruéjouls.

2.1. Hemp particles

Great care was taken here to produce different particle size distributions. Five categories of particles were produced : *Raw*, *Small Long*, *Large*, *Medium* and *Small*, as depicted in figure 1. The shives taken directly from the batch give the first category (*Raw*). Two techniques were used to obtain additional distributions : a 400 mm diameter vibratory sieving and a cutting mill (Retsch SM 300). At first, a 2.2 *mm* sieve was used to separate the *Raw* particles in two categories (*Small Long*, under the sieve and *Large* above the sieve). Two additional categories were obtained above the sieve after grinding. A 4 or 10 mm strainers and 2.2 *mm* or 1.6 *mm* sieves were used respectively for the *Medium* and *Small* categories (Fig. 1).

Approximately 500 *g* of hemp shives were loaded for each sieving with a vibration time of 5 minutes. The moisture content of the different particle size distributions was determined by batch of 200 *g*, by weighting before and after oven drying at 105°C during 72 hours (balance Minebea intec with a precision of 0.1 *g*). The average moisture content was 12%± 0.5%, dry basis.

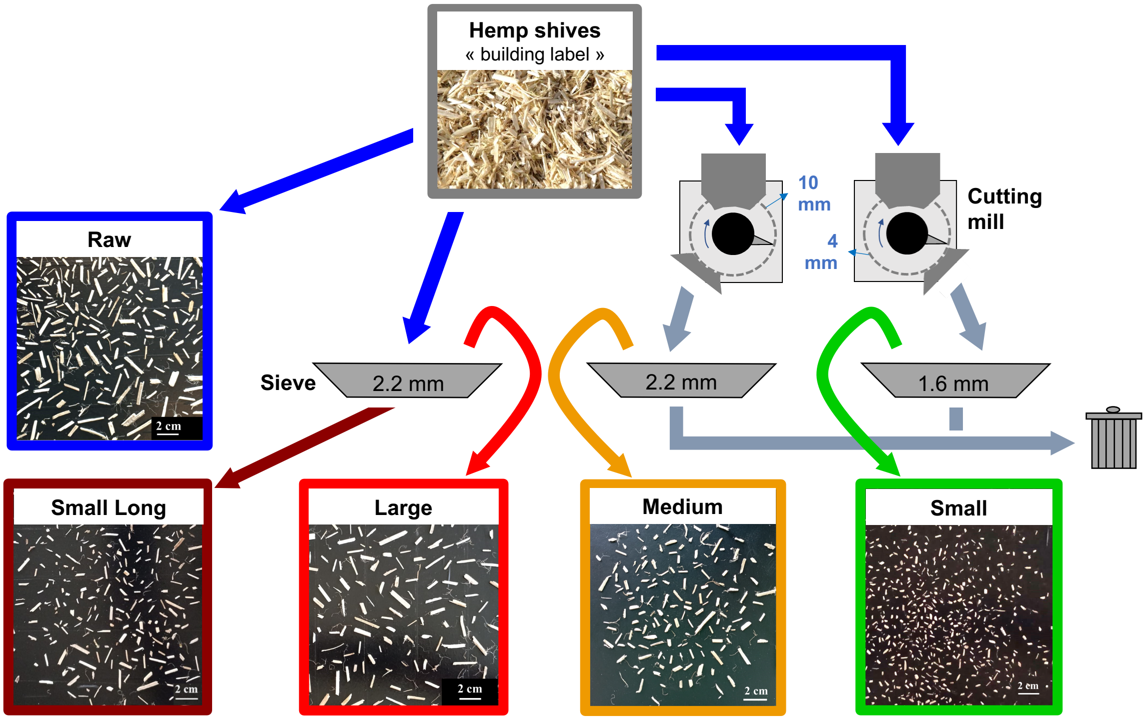

Figure 1: Method used to obtain different particle size distributions of hemp shives.

The geometrical characteristics of particles were assessed by image processing. At first, images were grabbed by a camera fixed 50 *cm* above the surface where particles were spread. The size distribution of each category was analyzed over a minimum of 1000 particles following a sampling method ensuring the representativity of the stock (Nguyen, 2010). Using *ImageJ* software (release 1.53), the original image was first converted to a binary image by the "Default" automatic thresholding function of *ImageJ*. The "Analyze Particle" tool was then used to measure the area and the major and minor axes of the "best-fit ellipse" of each particle. These axes were respectively considered as the length and width of the particle. Particles with an area less than 0.5 mm^2 were discarded. This includes dust and fine particles that represented less than 2% of the total particle area.

The thickness of the hemp particles, the third dimension that was not measured by image processing, was estimated using a digital caliper, with an accuracy of 0.01 *mm* on a sub-sample of all categories. The thickness was found to be closer to 1.00 *mm*, with a narrow distribution within and among categories (± 25%).

2.2. Fabrication of materials

The materials were manufactured following a design of experiment. The formulations varied by size of the hemp shives (the 5 categories presented in the previous section), but also by the Binder/Particle mass ratio (B/P : 1, 1.5 and 2) and by the target density (300, 400 and 500 $kg.m^{-3}$) by controlling the compaction pressure. A central composite design was used to chose the sets of parameters. This design of experiment is schematized in figure 2 and fully described in table 1. To limit the number of realizations, the design is complete only for the category "*Raw*". The design is incomplete for the other categories. The category "*Small-Long*" was used only for the central point (density of 400 $kg.m^{-3}$ and central Binder/Particle ratio of 1.5). Indeed, this realization is mainly intended to check the effect of particle elongation on the mechanical properties (another work in progress). For each project, the appropriate compaction method was chosen to obtain the targeted density: respectively 5, 13 and 1 formulations for *Low*, *Middle* and *High* compaction, as mentioned in figure 2 and detailed in the last column of table 1.

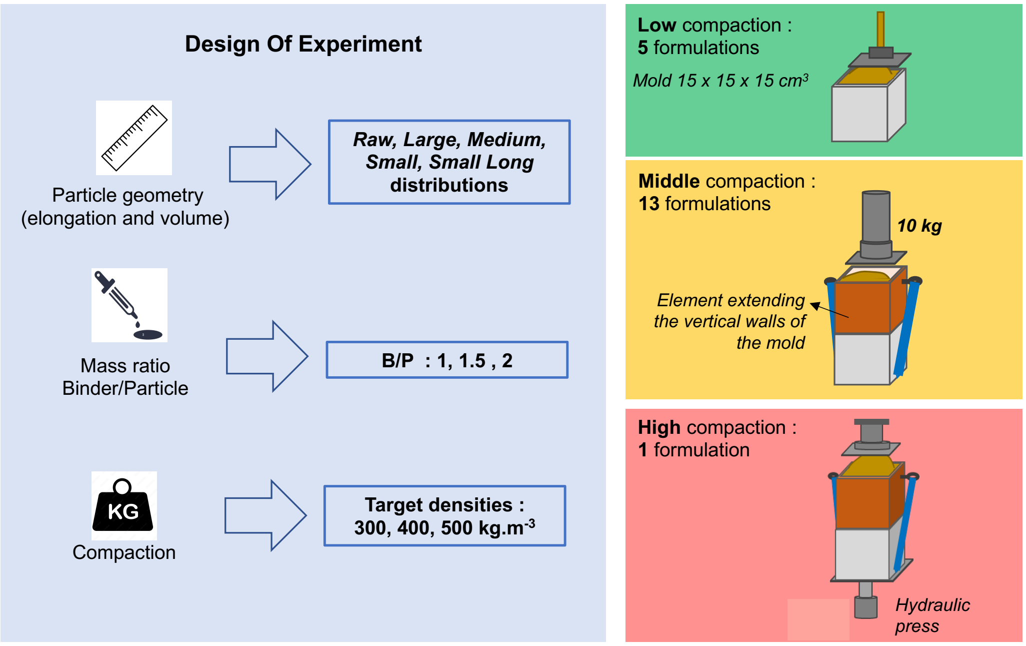

Figure 2: Design of experiment (left) and compaction method (right)

Particular attention was paid to the incorporation of water during the manufacture of the LHC. The objective is to minimize the mobility of the materials during setting (the source of many adhesion problems at the interfaces) while ensuring a sufficient quantity of water for the hydration of the binder, both of which are essential for good mechanical strength of the material. To that purpose, 170% of water in relation to the particle mass at ambient conditions (12% moisture content, db) was used for prewetting the particles. Following the supplier's recommendations, 40% of additional water in relation to the binder mass was used as mixing water. Finally, an extra 20% of the particle mass was added, in anticipation of further water absorption by the particles in the fresh mix during hydration of the binder. These quantities of water proportional to the particle mass (170 % pre-wetting and 20 % extra), were determined according to reference imbibition curves (Nozahic, 2012).

Methyl Hydroxyethyl Cellulose was added to the mixing water (2% w/w) to reduce mass mobility (water and extractibles) in the mixture and thus reduce concrete setting problems.

Table 1: Design of experiment

Category number	Particle category	Binder/Part. (B/P)	Density ($kg.m^{-3}$)			Compaction
			Target	Measured		
				along	across	
1	Raw	1	300	298.4	292.4	middle
2	Raw	1	400	404.5	416.1	middle
3	Raw	1	500	470.1	466.8	high
4	Raw	1.5	300	307.8	333.4	low
5	Raw	1.5	400	432.4	418.3	middle
6	Raw	1.5	500	485.9	468.9	middle
7	Raw	2	300	319.3	322.4	low
8	Raw	2	400	426.2	415.1	low
9	Raw	2	500	485.4	483.7	middle
10	Large	1	400	337.1	314.6	middle
11	Large	1.5	400	354.2	392.1	middle
12	Large	2	400	409.3	398.5	middle
13	Medium	1	400	397.4	403.8	middle
14	Medium	1.5	400	416.5	419.2	middle
15	Medium	2	400	419.4	424.2	low
16	Small	1	400	391.3	396.0	middle
17	Small	1.5	400	404.6	406.8	middle
18	Small	2	400	419.5	403.3	low
19	Small-Long	1.5	400	394.0	399.5	middle

The manufacturing process consisted first of pre-wetting the particles for 5 minutes using the horizontal shaft mixer (3R manufacturer). This mixer was used throughout the production process. At the same time, the Methyl Hydroxyethyl Cellulose was mixed with the mixing water using a kitchen mixer. Finally, the binder and mixing water were added to the pre-wetted particles and mixed for 8 minutes. All masses, calculated to obtain the target densities (Table 1), were measured using a balance with an accuracy of 1 g (Minebea intec). The moulds, $15 \times 15 \times 15\ cm^3$, were chosen in accordance with the NF EN 12 390-3 standard (Afnor, 2019). The mixture was placed in the molds and compacted using different techniques depending on the formulation

(Fig. 2). The procedure was repeated three times for each molding, superimposing three layers of 5 cm height. A scraping was performed between each layer to ensure a good adherence. Demoulding was carried out after 30 minutes. Samples were then stored in a humid room for 48 hours, at approximately 70% relative humidity and 20 °C. After this period, the specimens were stored in ambient conditions, at approximately 50% relative humidity and 20 °C. The density of specimens, stored at ambient conditions, was determined using a balance with accuracy of 1 g (Minebea intec) and a digital caliper of precision 0.1 mm.

2.3. Measurement of thermal conductivity

The thermal conductivity was measured in steady-state according to NF EN 12664:2001 standard (Afnor, 2001). The fluxmeter device is equipped with temperature controlled plates of $50 \times 50\ cm^2$ and two fluxmetric sensors (Captec) of size $10 \times 10\, cm^2$ and sensitivities of 0.0498 and 0.0655 $mV/(W.m^{-2})$ (calibrated values from the manufacturer). These fluxmeters were set on both sides of the specimen (Fig. 3). A temperature difference of 10 °C was applied to the sample by maintaining 15 °C on the back side and 25 °C on the front side. For the measurement of thermal conductivity, the heat fluxes were measured after the steady state was reached.

The samples were prepared with a dimension of $15 \times 15 \times 5\ cm^3$ (Fig. 3). Special attention was paid to the flatness of the samples by sanding them after sawing. Together with the fluxmeter surface, this guarantees a representative thermal conductivity value despite the heterogeneity of the material, whose representative size is that of the particles. The sample mass was measured with a 0.01 g precision balance (ADAM PGW 753e) and their thicknesses was measured at 4 points with a digital caliper (precision 0.1 mm). Before the conductivity measurement, the samples were dried in an oven at 60 °C until their mass was stabilized. The mass was kept stable during the measurement by the use of a thin cellulose hydrate film, type "Cellophane". In order to assess the moisture content during the test, the samples were weighted before the conductivity measurements and then after drying at 105 °C (after mass stabilization).

It is well-known that compaction influences the particles orientation in vegetable concrete: by a simple geometrical effect due to deformation, the particles tend to be oriented perpendicularly to the compaction direction. A compaction pressure of 0.1 MPa is already sufficient to produce a LHC with particles assumed to be globally oriented (de Bruijn et al., 2009). It is therefore very important to properly define the direction of the heat flux during thermal conductivity measurement (Fig. 3). In the following, two orientations are defined:

- The direction "across", when the imposed temperature gradient is parallel to the direction of compaction,
- The direction "along", when the imposed temperature gradient is orthogonal to the direction of compaction.

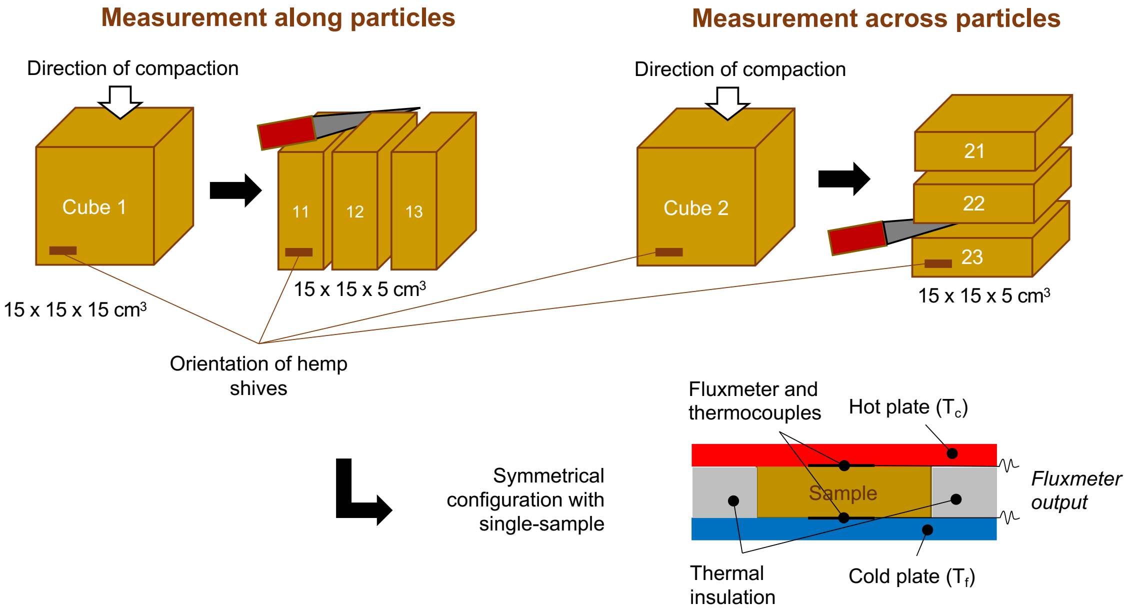

Figure 3: Sampling and flowmeter configuration for the directional measurement of thermal conductivity.

2.4. Morphological observation

The 3D morphology of the samples was observed by micro-tomography (Easy Tom XL Ultra 150-160, by RX Solutions). The microfocal source (150 kW, 75 W, 5 μm) and an amorphous silicon array sensor were used as compromise between sample size and spatial resolution. The acquisition protocol was as follows: 1568 projections at a voltage of 40 kV and a current of 500 μA and an exposure time of 5 seconds. The total scanning time was over 2 hours. The resolution of the reconstructed 3D image is 20 μm. Cylinders with a diameter of 40 mm and a length of about 2.5 cm were imaged. The axis of the cylinder is perpendicular to the orientation of particles.

The images were processed using the software Avizo, version 2019. A thresholding was applied first to separate the binder from the two other light phases (particles and pores). The threshold value was adjusted manually to obtain a fraction of binder phase in relation to actual phase volumes as calculated from the manufacturing conditions. Once done, objective parameters such as the number of binder clusters and their volumes could be obtained with the image processing software.

For a more accurate observation of the interface, the surface morphology of selected samples was observed using an environmental scanning electronic microscope (ESEM, FEI Quanta 200). Before imaging, the samples were delicately split by hand. Samples were fixed on the aluminum stub using a double-side carbon tape. The images were obtained without coating with the following conditions : secondary electrons detector, low vacuum mode, pressure of 110 Pa, voltage of 12.5 kV, spot size of 4, and a working distance of about 12 mm.

2.5. Data processing and model

All data were processed by custom R scripts (release 4.2.2) using the IDE RStudio (Version 2022.12.0). For each sample, the respective volumetric ratios of each phase (particles ε_p, binder ε_b and air ε_a) are computed using the densities of phases (air density ρ_a, particle density ρ_p and binder density ρ_b), the sample density ρ_{sample} and the Binder/Particle mass ratio (R_{BP}) as follows:

$$\varepsilon_p = \frac{\rho_{sample} - \rho_a}{\rho_p(1 + R_{BP}) + \rho_a(1 + \rho_p/\rho_b R_{BP})} \tag{1}$$

$$\varepsilon_b = \frac{\varepsilon_p \rho_p R_{BP}}{\rho_b} \tag{2}$$

$$\varepsilon_a = 1 - \varepsilon_p - \varepsilon_b \tag{3}$$

The intrinsic density of hemp shives cell wall is about 1450 $kg.m^{-3}$ according to (Barbieri et al., 2020) and the apparent density of a particle ρ_p of 300 $kg.m^{-3}$ was reported in the literature (Barbieri et al., 2020; Jiang et al., 2021). Measurements performed on some of our particles confirmed this order of magnitude. For this density, the thermal conductivity of particles λ_p is considered to be 0.08 $W.m^{-1}.K^{-1}$ (Yu et al., 2011). According to the manufacturer, the density of the hydrated binder matrix (without aggregate), ρ_b, previously mixed with 40% w/w of mixing water is approximately 1300 $kg.m^{-3}$, with a thermal conductivity λ_b of 0.7 $W.m^{-1}.K^{-1}$. The density of air is set to 1.2 $kg.m^{-3}$ and its conductivity to 0.024 $W.m^{-1}.K^{-1}$.

Theoretically, the macroscopic, or effective property, can be predicted by homogenization from the properties of each phase, their proportion and morphology (Sanchez-Palencia, 1983; Allaire, 1992; Hornung, 1997; Perré, 2007, 2010). This strategy becomes predictive provided that the phase properties are known and the real 3D morphology is described with sufficient accuracy over a Representation Elementary Volume (REV). This was successfully applied to thermal conductivity (Wang and Pan, 2008; Wulf et al., 2014; Fang et al., 2016; Louërat et al., 2018; Quenjel and Perré, 2022). The 3D morphology is however difficult to define for vegetable concrete for two reasons:

- segmentation of 3D µ-tomography images is difficult due to the low contrast between the pores and the hemp particles,
- the trade-off between the size of the REV (Representative Elementary Volume) and the resolution required to define the local morphology is very difficult for particles that can be up to a few centimeters long.

Instead, the present work proposes a global approach, based on the extreme values that can be obtained theoretically with the respective volumes of the three phases : the series model $\lambda_\perp$ and the parallel model $\lambda_\parallel$:

$$\lambda_\perp = (\varepsilon_a \lambda_a^{-1} + \varepsilon_p \lambda_p^{-1} + \varepsilon_b \lambda_b^{-1})^{-1} \tag{4}$$

$$\lambda_\parallel = \varepsilon_a \lambda_a + \varepsilon_p \lambda_p + \varepsilon_b \lambda_b \tag{5}$$

For any heterogeneous medium, the effective value is necessarily between these two limits. Mixture laws can be use to define the actual value inside this interval by one global parameter μ:

$$\lambda_{actual} = (\varepsilon_a \lambda_a^\mu + \varepsilon_p \lambda_p^\mu + \varepsilon_b \lambda_b^\mu)^{1/\mu} \tag{6}$$

Equation (6) is convenient as the series model is obtained with $\mu = -1$ and the parallel model with $\mu = 1$. It has been proposed successfully to propose predictive expressions (Perré and Turner, 2001; Louërat et al., 2018). Yet, the singularity at $\mu = 0$ was problematic in the analysis proposed hereafter.

Instead, the measured value λ_{meas} was defined as a fraction, $f_\parallel$, of the series model in a weighed averaged of the two extreme values:

$$\lambda_{meas} = f_\parallel \lambda_\parallel + (1 - f_\parallel)\lambda_\perp \tag{7}$$

This fraction $f_\parallel$ can be computed for each sample from the measured values, in both directions, using equations (1) to (3) and (7).

3. Results

3.1. Size distribution of hemp shives

Figure 4 and table 2 summarize the particle size distribution of the 5 categories used to manufacture the materials. These values were obtained from a random sample of ca. 1000 particles. The distributions of figure 4 are distributions weighted by the particle area. As the particle thickness varies over a narrow range, the particle area is a good proxy of the proportion of biomass volume, the relevant parameter to understand the material properties. Consistently, the average values and standard deviations of table 2 are also weighted values, computed using the following formula :

$$\bar{x} = \frac{\sum_{i=1}^{N} w_i x_i}{\sum_{i=1}^{N} w_i} \qquad \text{and} \qquad \sigma = \sqrt{\frac{\sum_{i=1}^{N} w_i (x_i - \bar{x})^2}{\frac{(N-1)}{N} \sum_{i=1}^{N} w_i}} \tag{8}$$

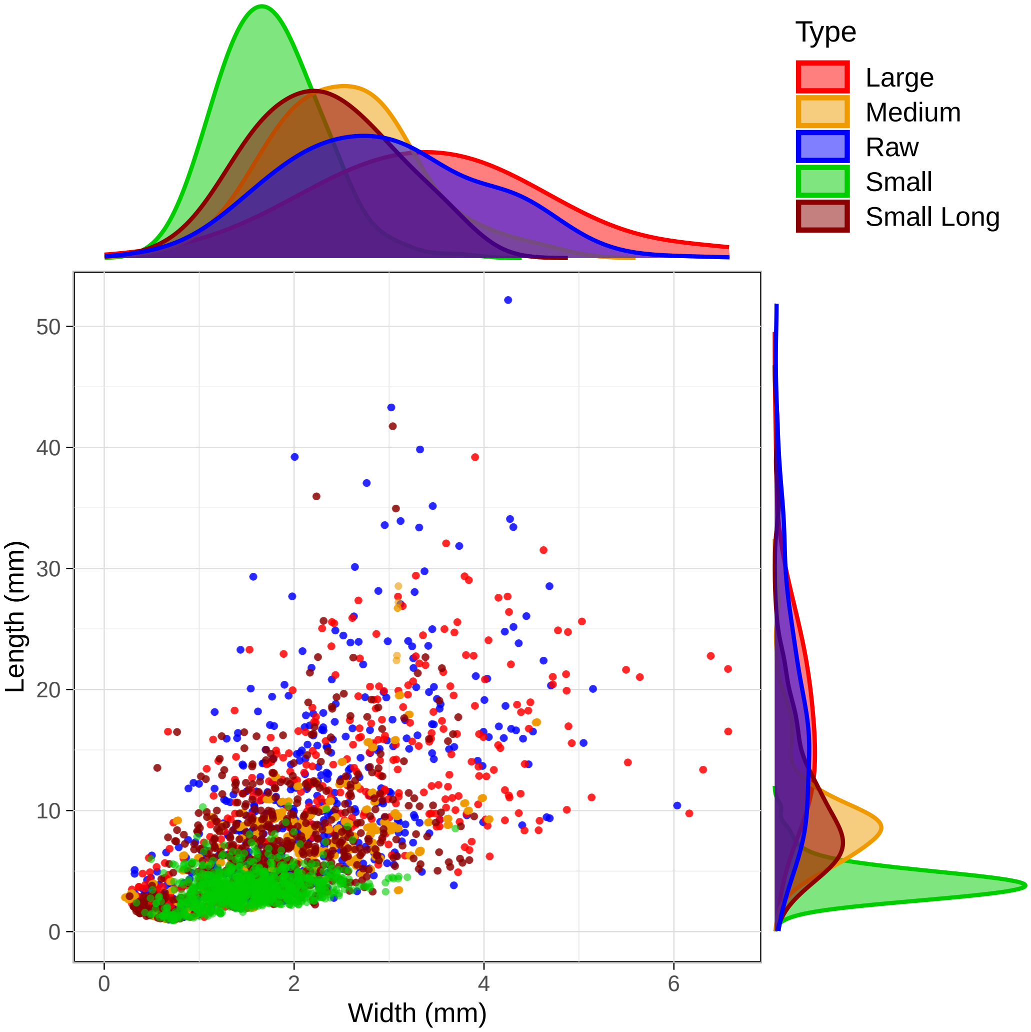

Figure 4: Geometric characteristics of hemp shives : scatter plot with side plots of width and length distribution weighted by the particle area.

Unsurprisingly, the *Raw* distribution depicts large dispersion values, both in length and diameter with rather high average values : 2.9 mm and 17.9 mm respectively for width and length. The *Small long* and *Large* distributions are two fractions of the *Raw* particles, after separation by sieving (see figure 1). The *Large* category, recovered above the sieve, is the largest fraction of *Raw* : its width is significantly shifted to the right in figure 4, with an average width of 3.5 mm instead of 2.9 mm for *Raw*, while they present a similar length as *Raw*, but with a narrowest length distribution. Consistently, the *Small Long* has its distributions (both width and length) shifted to lower values (resp. 2.3 and 11.5 mm for the average values). Finally, the combination of grinding and sieving allowed two additional categories to be obtained : *Medium* and *Small*. These two categories are obviously characterized by medium and small sizes (respectively 2.5 and 1.7 mm for the width and 9.8 and 4.2 mm for the length). Grinding and sieving also produced smaller elongations (respectively 4.0 and 2.6) compared to the three first categories that depict similar elongation values (6.3, 5.2 and 5.4).

Table 2: Means and standard deviations of particle size distributions of hemp shives, weighted by the particle surface.

Category	Area Mean(SD) mm^2	Length Mean(SD) mm	Width Mean(SD) mm	Elong. Mean(SD) -	Dust* Fraction -
Raw	57.0 (42.6)	17.9 (10.1)	2.9 (1.0)	6.3 (3.2)	1.0%
Small Long	22.1 (18.2)	11.5 (7.2)	2.3 (0.7)	5.2 (3.0)	1.5%
Large	49.3 (28.2)	17.4 (6.9)	3.5 (1.2)	5.4 (2.4)	0.8%
Medium	20.8 (14.2)	9.8 (4.4)	2.5 (0.7)	4.0 (1.6)	1.5%
Small	5.9 (3.2)	4.2 (1.5)	1.7 (0.5)	2.6 (1.2)	2.5%

Elong. = Elongation factor
SD = Standard Deviation
*Dust and particles smaller than 0.5 mm^2¿ (length x width)

3.2. Overview of thermal conductivity values

For each sample, the moisture content was determined by weighting just before the test and after oven-drying (see section 2.3). The moisture content was very similar for all samples, with an averaged value of 5.7 %, dry basis, and a standard deviation of 0.3 %. All experimental values of thermal conductivity are summarized in ternary diagrams (Fig. 5). In these graphs, the volume fractions of each phase are represented by the three axes, while the density is plotted as isovalues (red lines) and the measured conductivity as markers whose color is tied to value categories. It is interesting to observe that the residual porosity is very small (less than 10 %) for some realizations of the experimental design, which explains the need for higher compaction. In addition, on the same density line, it seems that increasing the binder phase increases the thermal conductivity, clearly visible along the iso-density lines whatever the direction.

Figure 6 plots all values as a function of density. The large dispersion proves that density alone is not able to correctly predict the thermal conductivity. In spite of this dispersion, the direction of measurement, along or across particles, is the only obvious trend than can be noticed from this graph.

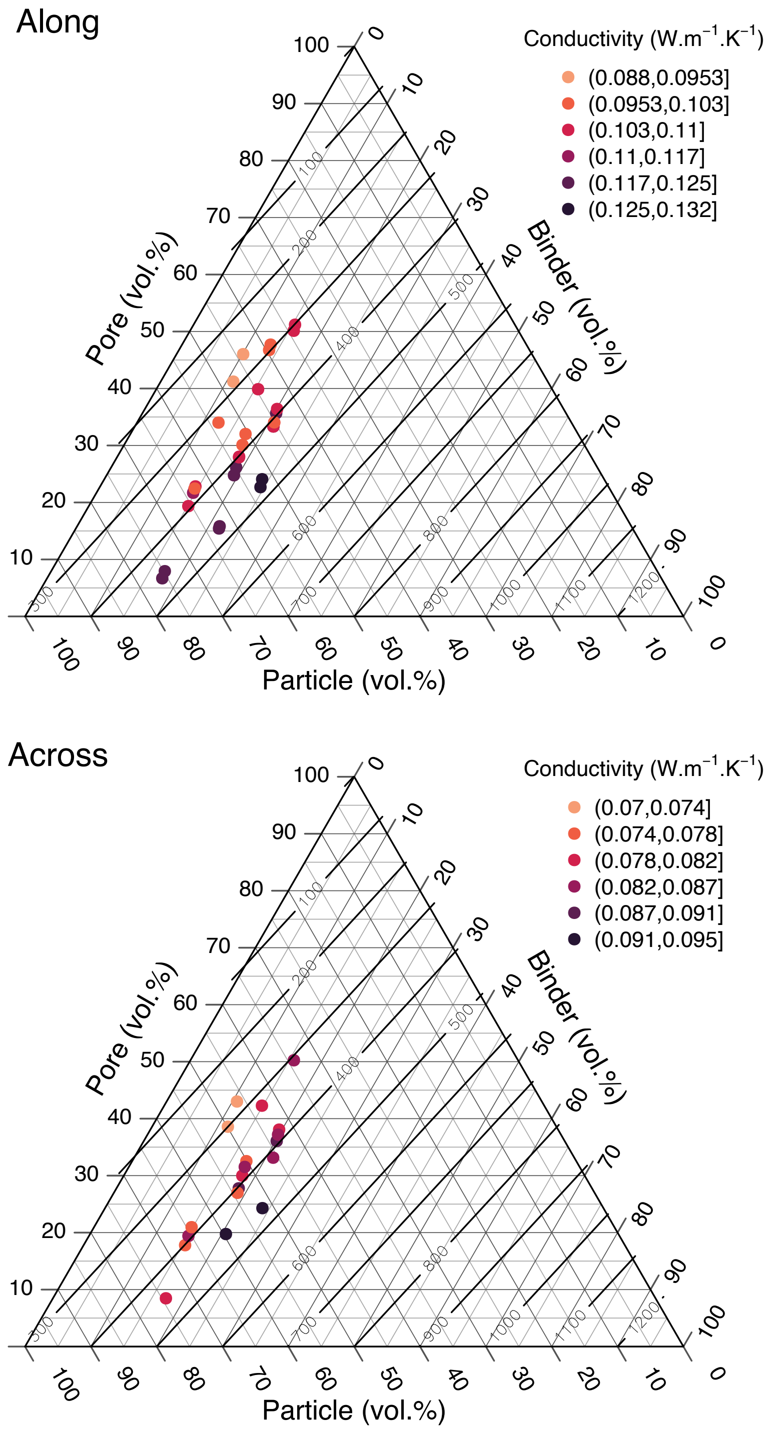

Figure 5: A global view of the design of experiment and the measured values of thermal conductivity, obtained along particles (top) and across particles (bottom). The red lines are density isovalues.

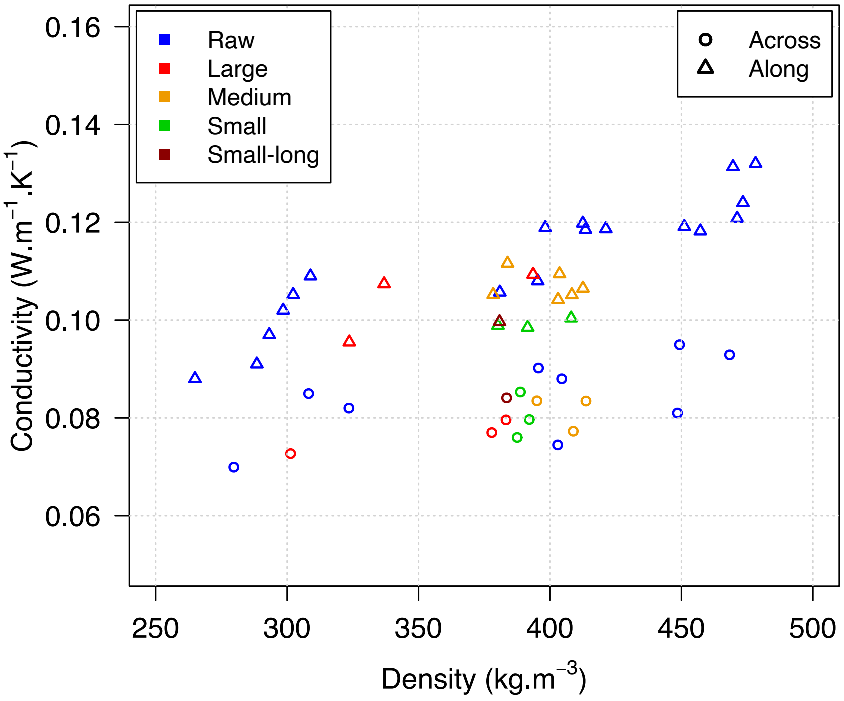

Figure 6: The measured conductivity values plotted as a function of density. In spite of the large dispersion, values across particles are globally lower than values along particles.

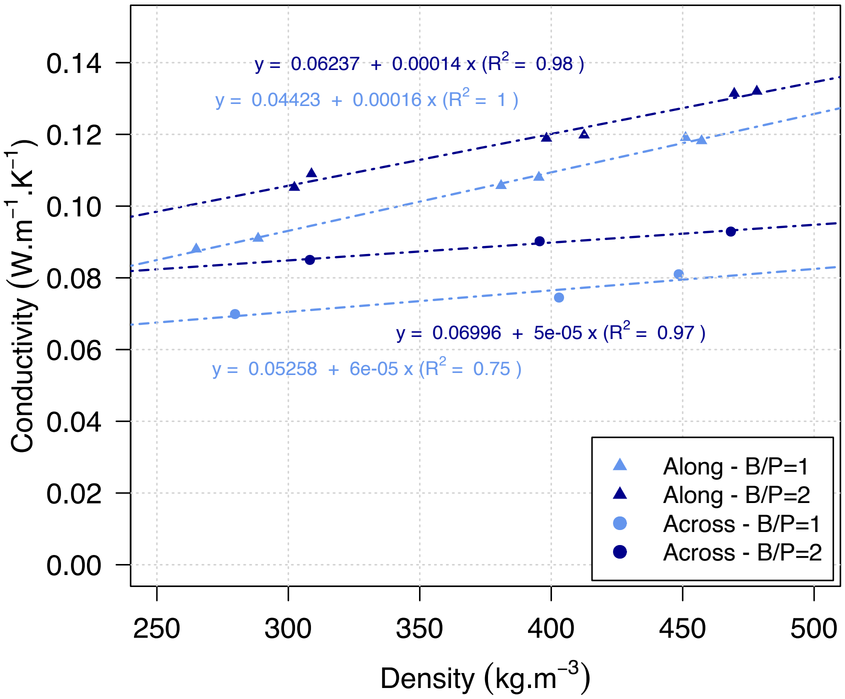

Figure 7: Reducing the dateset to subsets allows excellent correlations to be revealed for each direction (*Raw* distribution only for two binder/particle ratios).

This dispersion is mainly due to the richness of the database established on the basis of an experimental design. For the sake of example, figure 7 proves that the data scattering can be impressively reduced by focusing on a selected subset. This plot is restricted to materials manufactured with one single particle category (*Raw*) and two B/P ratios. For each ratio, the correlation is excellent in both directions: for a single B/P ratio and one particle category, the correlation between density and conductivity is excellent. However, these two subsets confirm that density alone is not a good predictor: at constant density, the thermal conductivity increases with the binder ratio. Indeed, at constant density, a larger amount of particles is required at low B/P ratio due to the contrast of density of these phases (300 $kg.m^{-3}$ against 1450 $kg.m^{-3}$). However, the contrast of thermal conductivity is even larger (0.08 $W.m^{-1}.K^{-1}$ against 0.7 $W.m^{-1}.K^{-1}$). The later over-compensates for the contrast of density and explains why the thermal conductivity of the material is eventually smaller for a low B/P ratio.

Obtaining a predictive model capable of handling the whole database is more challenging, but is necessary to better understand the combined effects of all the parameters. This is the purpose of the remaining content of this paper.

4. Predictive model

4.1. Effect of porosity on phase morphology

The formulation described in equations (1), (3) and (7) accounts for the contribution of all phases to the macroscopic conductivity. However, this formulation requires the fraction $f_{\|}$ of the parallel model, a synthetic indicator of the phase arrangement, to be obtained somehow to propose a predictive model. This fraction was first computed for each sample and both directions from its experimental value of thermal conductivity thanks to equation (7). As expected, the parallel fraction $f_{\|}$ is larger along particles than across particles, which leads to higher thermal conductivity values. Note that the particles themselves are not the conductive phase. The effect of particle orientation of the product anisotropy is then indirect. In fact, the particles also structure the morphology of the binder, the most conductive phase, that surrounds the particles. The binder is therefore oriented in the same direction as the particles. The proportion of parallel model is then larger in the direction (*along*) than in the direction *across*. More surprisingly, this fraction tends to decrease with density for both directions. This result was not expected. The data were further analyzed and the best correlation was found when plotting the fraction of the parallel model as a function of the sample porosity. These results and the best fit linear correlations are summarized in figure 8. The correlation is rather good across particles ($R^2 = 0.81$) and a little looser along particles ($R^2 = 0.52$). As can be observed in figure 8, this is mainly explained by the categories *Small* and *Medium* which clearly deviate from the general trend in the direction
textitalong.

This interesting finding can be explained as follows. The conductivity tends to be high (closer to the parallel model) when the most conductive phase is connected. This was observed for wood for example, for which the property is close to the parallel model for thermal conduction (the connected cell wall is the conductive phase in this case). On the contrary, mass diffusivity is close to the series model as the gaseous, non-connected, phase is the most conductive phase (Perré et al., 2015). This is exactly what occurs during the manufacturing of concrete samples. The binder is mixed with the particles and therefore surrounds the particles. When the porosity is large, most of the binder, the most conductive phase, remains connected. On the contrary, when the porosity becomes too small, particles should be compacted during manufacturing. Therefore, the binder, which is not yet cured, is expelled into the residual porosity, thus loosening the connectivity of this phase. Thus, a mix that has undergone more compaction during its manufacture will have a reduced thermal conductivity in proportion of the potential conductivity of the ingredients, as the most conductive phase will be less connected. Consequently, the macroscopic value will be closer to the series model. Still, the binder continues to be oriented by the particles : the conductivity along particles remains larger than the conductivity across particles.

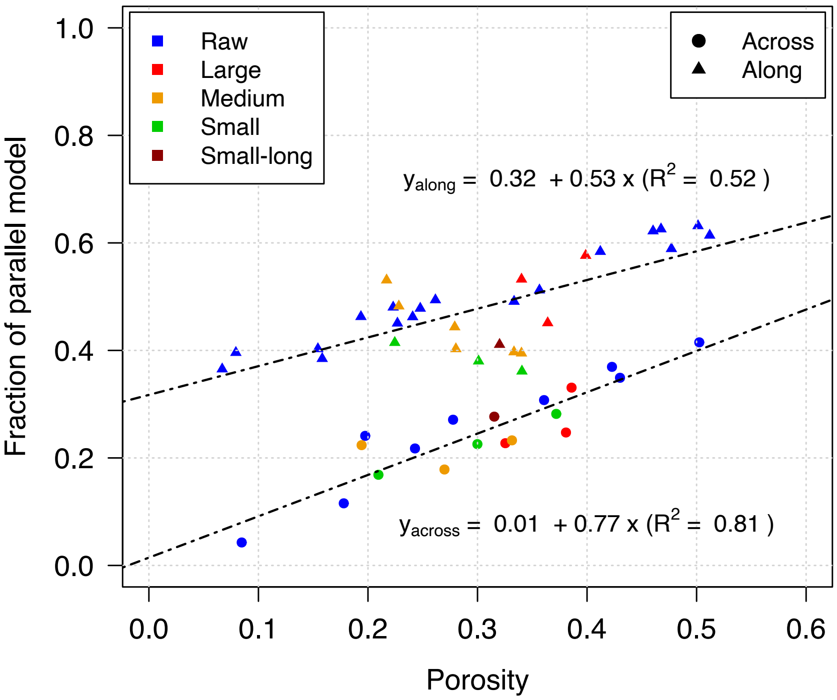

Figure 8: The fraction of parallel models computed from the measured value of conductivity for all samples and both directions. The plot depicts also the linear correlations fitted from these values. The upper images schematically show the effect of porosity on binder distribution.

To confirm this explanation, two contrasted formulations with a similar total amount of binder were observed by X-ray micro-tomography and ESEM (Fig. 9). The large binder ratio with low density (left side of figure 9) required a low compaction and has an important porosity. On the contrary, the low B/P ratio with large density needed a high compaction. The image clearly shows that particle coating by the binder is weaker and finer when compaction is high, i.e. at low porosity.

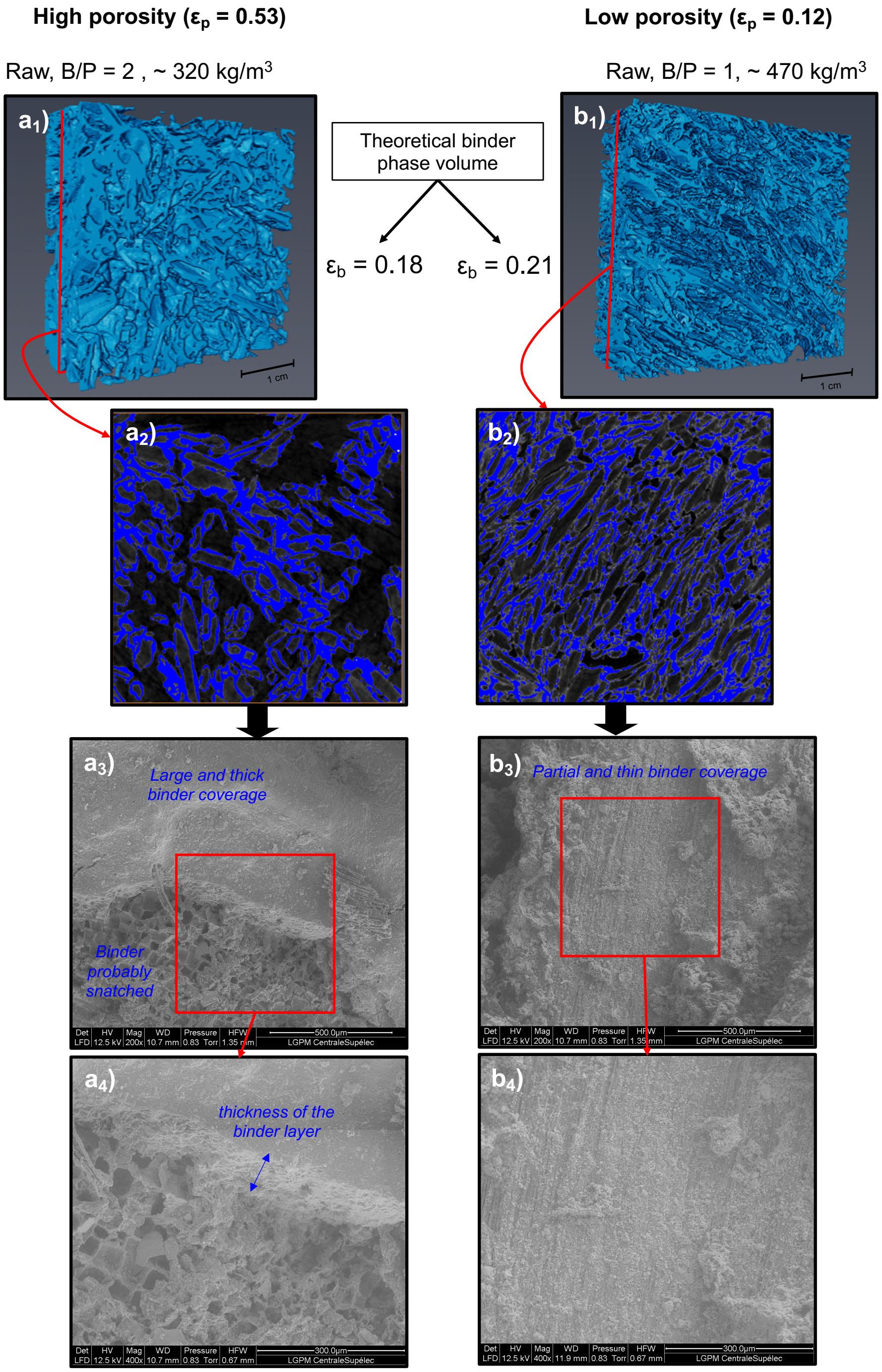

Figure 9: Observation of the microstructure and binder matrix distribution of the hemp-lime formulations - a) formulation high proportion of binder (B/P=2), low density (320 $kg.m^{-3}$) - b) formulation low proportion of binder (B/P=1), high density (470 $kg.m^{-3}$) - index 1: 3D reconstruction by X-Ray microtomography - index 2: selection of a 2D image from the 3D reconstruction - indexes 3 and 4: SEM observations, respectively at 200 and 400 zoom factor

Using the same thresholding method, 3D image processing yields a 6-fold increase in the total number of binder clusters for the densest formulation. This result clearly confirms that the connectivity of the binder phase is significantly reduced by compaction.

4.2. A predictive model

The linear fits between porosity and fraction of the series model was used to predict the thermal conductivity in both directions. Figure 10a depicts the values predicted as a function of measured values. The linear fit confirms that the slope is very close to the unit (0.96). Keeping in mind that all particles categories were considered together, the R^2 value (0.86) is very good as well. The predictions are excellent for all elongated particles (categories *Raw*, *Large* and *Small-Long*). On the contrary, the points furthest from the bisector are the values obtained for the particle shapes with the smallest elongations (*Medium* and *Small*). To better analyze these discrepancies, all values were plotted as a function of density (Fig. 10b). Large open markers are the measured values and small plain markers are the corresponding predicted values. Vertical lines were added to better depict the gap between measurement and prediction . This figure confirms that the model performs much better than simply using the density to predict conductivity. This is particularly evident in the case of the blue markers clustered around 300 $kg.m^{-3}$, for which the model predictions are nearly perfect despite the lack of correlation with density. More generally, the good prediction obtained for the elongated particles is confirmed over the entire range of density by the small gap between prediction and measurement for these categories. For thermal conductivity, it seems then that the particle elongation matters more than the particle size. As depicted in table 2, only the last category (*Small*) has a much lower elongation. As a consequence of this very low elongation, the conductivity is less anisotropic, as depicted by the significant difference between measurement and prediction, namely along particles. The *Medium* particle distribution depicts a behavior mid-way between *Small* and the other ones.

To ease the use of this predictive model, the complete formulation and numerical values are summarized hereafter:

$$\begin{aligned}\lambda_{across} &= f_{across}\lambda_{\perp} + (1 - f_{across})\lambda_{\parallel} \\ &\text{with } f_{across} = 0.01 + 0.77\,\varepsilon_a\end{aligned}$$

and

$$\begin{aligned}\lambda_{along} &= f_{along}\lambda_{\perp} + (1 - f_{along})\lambda_{\parallel} \\ &\text{with } f_{along} = 0.32 + 0.53\,\varepsilon_a\end{aligned}$$

In these equations, the product porosity ε_a and the extreme conductivity values $\lambda_{\parallel}$ and $\lambda_{\perp}$ are obtained with the following expressions and numerical values

$$\begin{aligned}\varepsilon_p &= \frac{\rho_{product} - \rho_a}{\rho_p(1 + R_{BP}) + \rho_a(1 + \rho_p/\rho_b R_{BP})} \\ \varepsilon_b &= \frac{\varepsilon_p \rho_p R_{BP}}{\rho_b} \\ \varepsilon_a &= 1 - \varepsilon_p - \varepsilon_b \\ \lambda_{\perp} &= (\varepsilon_a \lambda_a^{-1} + \varepsilon_p \lambda_p^{-1} + \varepsilon_b \lambda_b^{-1})^{-1} \\ \lambda_{\parallel} &= \varepsilon_a \lambda_a + \varepsilon_p \lambda_p + \varepsilon_b \lambda_b\end{aligned}$$

where

$$\begin{aligned}\rho_a &= 1.2\,kg.m^{-3}, &\qquad \lambda_a &= 0.024\,W.m^{-1}.K^{-1} \\ \rho_p &= 300\,kg.m^{-3}, &\qquad \lambda_p &= 0.08\,W.m^{-1}.K^{-1} \\ \rho_b &= 1300\,kg.m^{-3}, &\qquad \lambda_b &= 0.7\,W.m^{-1}.K^{-1}\end{aligned}$$

In the case of particles with very small elongation, the best prediction is obtained assuming the product to be isotropic:

$$f_{across} = f_{along} = 0.165 + 0.65\,\varepsilon_a$$

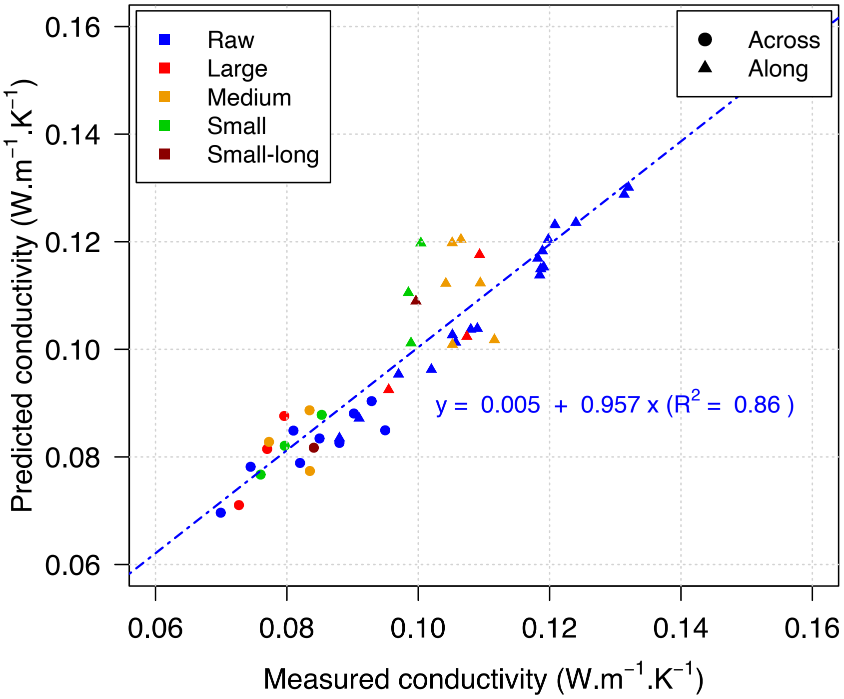

(a) Comparison between predicted and measured conductivities.

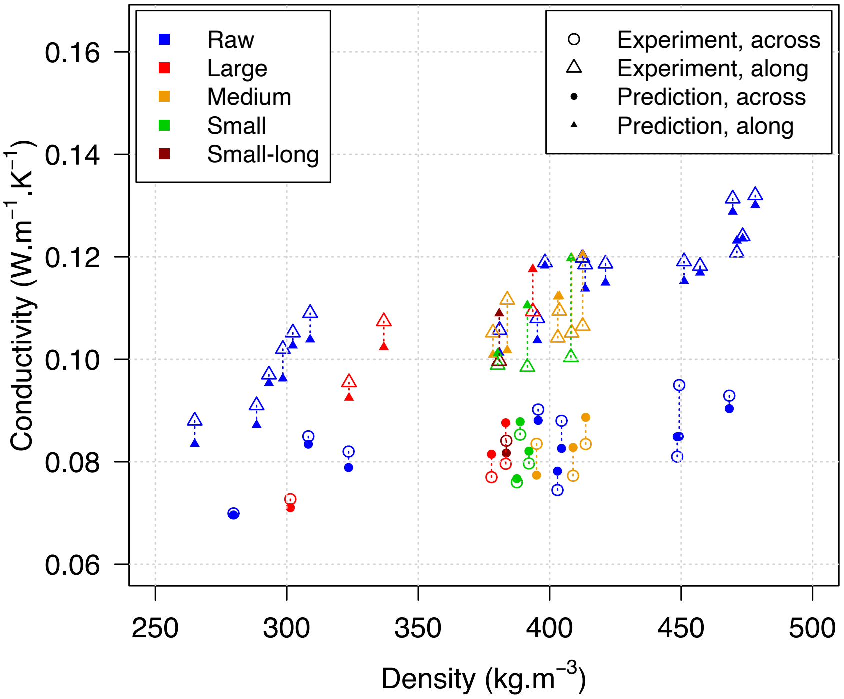

(b) Measured and predicted thermal conductivity as a function of density. Large open markers are the measured values and small plain markers are the predicted values.

Figure 10: The conductivity predicted by the model based on porosity as synthetic parameter.

5. Conclusion

This study investigated the thermal conductivity of lime-hemp concrete. Based on a Design of Experiment (DoE), a total of 19 material realizations were produced. Several parameters were systematically varied, including five particle categories (*Raw*, *Large*, *Medium*, *Small-long* and *Small*), three Binder/Particle ratios (1, 1.5 and 2) and three target densities (300, 400 and 500 $kg.m^{-3}$).

Overall, thermal conductivity along the particles (thermal gradient orthogonal to the direction of compaction) is higher than across the particles, with a factor ranging from 1.25 to 1.5. When dealing with subsets of constant binder/particle ratio and for a single particle category, density is able to nicely predict the thermal conductivity, providing a different expression for each direction. On the contrary, density alone is not a good indicator of the macroscopic value. As main challenge of this work, a novel approach, based on the material porosity, was proposed and successfully tested to predict the conductivity over the very wide range of material realizations provided by our DoE. This success is explained by the effect of porosity on the material morphology, namely the connectivity of the binder. The effect of particle size distribution depends on the particle elongation rather than the particle size. This is why the conductivity of the category *Small*, which has also the lowest elongation, is almost isotropic. Expressions are proposed for predicting conductivity from readily available macroscopic characteristics (proportions, densities and conductivities of the gas, hemp and binder phases). These expressions are likely to be relevant for other types of vegetable concretes.

Acknowledgment

Communauté Urbaine du Grand Reims, Département de la Marne, Région Grand Est and European Union (FEDER Champagne-Ardenne 2014-2020) are acknowledged for their financial support to the Chair of Biotechnology of CentraleSupélec and the Centre Européen de Biotechnologie et de Bioéconomie (CEBB).

References

Afnor, 2001. NF EN 12664 : Performance thermique des matériaux et produits pour le bâtiment - Détermination de la résistance thermique par la méthode de la plaque chaude gardée et la méthode fluxmétrique - Produits secs et humides de moyenne et basse résistance thermique.

Afnor, 2019. NF EN 12390-3: Essai pour béton durci - partie 3 : résistance à la compression des éprouvettes .

Allaire, G., 1992. Homogenization and two-scale convergence. SIAM Journal on Mathematical Analysis 23, 1482–1518.

Arnaud, L., Gourlay, E., 2012. Experimental study of parameters influencing mechanical properties of hemp concretes. Construction and Building Materials 28, 50–56. doi:10.1016/j.conbuildmat.2011.07.052.

Asli, M., Brachelet, F., Sassine, E., Antczak, E., 2021. Thermal and hygroscopic study of hemp concrete in real ambient conditions. Journal of Building Engineering 44, 102612. doi:10.1016/j.jobe.2021.102612.

Barbieri, V., Lassinantti Gualtieri, M., Siligardi, C., 2020. Wheat husk: A renewable resource for bio-based building materials. Construction and Building Materials 251, 118909. doi:10.1016/j.conbuildmat.2020.118909.

Benmahiddine, F., Bennai, F., Cherif, R., Belarbi, R., Tahakourt, A., Abahri, K., 2020. Experimental investigation on the influence of immersion/drying cycles on the hygrothermal and mechanical properties of hemp concrete. Journal of Building Engineering 32, 101758. doi:10.1016/j.jobe.2020.101758.

Bennai, F., Ferroukhi, M.Y., Benmahiddine, F., Belarbi, R., Nouviaire, A., 2022. Assessment of hygrothermal performance of hemp concrete compared to conventional building materials at overall building scale. Construction and Building Materials 316, 126007. doi:10.1016/j.conbuildmat.2021.126007.

Boutin, C., 1996. Conductivité thermique du béton cellulaire autoclavé: modélisation par méthode autocohérente. Materials and Structures 29, 609–615. doi:10.1007/BF02485968.

Brzyski, P., Gleń, P., Gładecki, M., Rumińska, M., Suchorab, Z., Łagód, G., 2021. Influence of the Direction of Mixture Compaction on the Selected Properties of a Hemp-Lime Composite. Materials 14, 4629. doi:10.3390/ma14164629.

Cerezo, V., 2005. Propriétés mécaniques, thermiques et acoustiques d'un matériau à base de particules végétales : approche expérimentale et modélisation théorique. Ph.D. thesis.

Collet, F., Chamoin, J., Pretot, S., Lanos, C., 2013. Comparison of the hygric behaviour of three hemp concretes. Energy and Buildings 62, 294–303. doi:10.1016/j.enbuild.2013.03.010.

Collet, F., Prétot, S., 2014. Thermal conductivity of hemp concretes : Variation with formulation, density and water content. Construction and Building Materials 65, 612–619. doi:10.1016/j.conbuildmat.2014.05.039.

Costantine, G., Maalouf, C., Moussa, T., Kinab, E., Polidori, G., 2020. Hygrothermal evaluation of hemp concrete at wall and room scales: Impact of hysteresis and temperature dependency of sorption curves. J. Build Phys. 44, 183–224. doi:10.1177/1744259119896380.

Dartois, S., Mom, S., Dumontet, H., Ben Hamida, A., 2017. An iterative micromechanical modeling to estimate the thermal and mechanical properties of polydisperse composites with platy particles: Application to anisotropic hemp and lime concretes.

Construction and Building Materials 152, 661–671. doi:10.1016/j.conbuildmat.2017.06.181.

Fang, W.Z., Chen, L., Gou, J.J., Tao, W.Q., 2016. Predictions of effective thermal conductivities for three-dimensional four-directional braided composites using the lattice Boltzmann method. Int. J. Heat Mass Transfer 92, 120–130. doi:10.1016/j.ijheatmasstransfer.2015.08.071.

Florentin, Y., Pearlmutter, D., Givoni, B., Gal, E., 2017. A life-cycle energy and carbon analysis of hemp-lime bio-composite building materials. Energy Buildings 156, 293–305. doi:10.1016/j.enbuild.2017.09.097.

Gourlay, E., Glé, P., Marceau, S., Foy, C., Moscardelli, S., 2017. Effect of water content on the acoustical and thermal properties of hemp concretes. Construction and Building Materials 139, 513–523. doi:10.1016/j.conbuildmat.2016.11.018.

Gündüz, Y., Şahin, Y., 2021. Relation of the Thermal Conductivity and the Electrical Resistivity to the Unit Weight of Hemp Based Composites. Int J Thermophys 42, 103. doi:10.1007/s10765-021-02857-2.

Haik, R., Peled, A., Meir, I.A., 2020. The thermal performance of lime hemp concrete (LHC) with alternative binders. Energy Build. 210, UNSP 109740. doi:10.1016/j.enbuild.2019.109740.

Hajj Obeid, M., Douzane, O., Freitas Dutra, L., Promis, G., Laidoudi, B., Bordet, F., Langlet, T., 2022. Physical and Mechanical Properties of Rapeseed Straw Concrete. Materials 15, 8611. doi:10.3390/ma15238611.

Hajmohammadian Baghban, M., Hovde, P.J., Jacobsen, S., 2013. Analytical and experimental study on thermal conductivity of hardened cement pastes. Materials and Structures 46, 1537–1546. doi:10.1617/s11527-012-9995-y.

Hornung, U. (Ed.), 1997. Homogenization and Porous Media. Springer–Verlag, New York.

Huang, G., Abou-Chakra, A., Geoffroy, S., Absi, J., 2023. A multiscale homogenization model on thermal conductivity of bio-based building composite considering anisotropy, imperfect interface and moisture. Construction and Building Materials 377, 131156. doi:10.1016/j.conbuildmat.2023.131156.

IEA, 2017. World Energy Outlook 2017 – Analysis. Technical Report.

IEA, 2021. Buildings 2021 – Analysis. Technical Report.

Jiang, Y., Lawrence, M., Ansell, M.P., Hussain, A., 2021. Cell wall microstructure, pore size distribution and absolute density of hemp shiv. Royal Society Open Science 5, 171945. doi:10.1098/rsos.171945.

Liu, M., Fernando, D., Daniel, G., Madsen, B., Meyer, A.S., Ale, M.T., Thygesen, A., 2015. Effect of harvest time and field retting duration on the chemical composition, morphology and mechanical properties of hemp fibers. Industrial Crops and Products 69, 29–39. doi:10.1016/j.indcrop.2015.02.010.

Louërat, M., Ayouz, M., Perré, P., 2018. Heat and moisture diffusion in spruce and wood panels computed from 3-D morphologies using the Lattice Boltzmann method. Int. J. of Thermal Sciences 130, 471–483. doi:10.1016/j.ijthermalsci.2018.05.009.

Magniont, C., Escadeillas, G., Coutand, M., Oms-Multon, C., 2012. Use of plant aggregates in building ecomaterials. European Journal of Environmental and Civil Engineering 16, s17–s33. doi:10.1080/19648189.2012.682452.

Nguyen, S.T., Tran-Le, A.D., Vu, M.N., To, Q.D., Douzane, O., Langlet, T., 2016. Modeling thermal conductivity of hemp insulation material: A multi-scale homogenization approach. Building and Environment 107, 127–134. doi:10.1016/j.buildenv.2016.07.026.

Nguyen, T.T., 2010. Contribution à l'étude de la formulation et du procédé de fabrication d'éléments de construction en béton de chanvre. Ph.D. thesis. Université de Bretagne Sud.

Nozahic, V., 2012. Vers une nouvelle démarche de conception des bétons de végétaux lignocellulosiques basée sur la compréhension et l'amélioration de l'interface liant / végétal : application à des granulats de chenevotte et de tige de tournesol associés à un liant ponce / chaux. Ph.d. thesis. Clermont-Ferrand 2.

Oumeziane, Y.A., Moissette, S., Bart, M., Lanos, C., 2016. Influence of temperature on sorption process in hemp concrete. Construction and Building Materials 106, 600–607. doi:10.1016/j.conbuildmat.2015.12.117.

Page, J., Sonebi, M., Amziane, S., 2017. Design and multi-physical properties of a new hybrid hemp-flax composite material. Construction and Building Materials 139, 502–512. doi:10.1016/j.conbuildmat.2016.12.037.

Perré, P., 2007. Multiscale aspects of heat and mass transfer during drying. Drying of Porous Materials , 59–76.

Perré, P., 2010. Multiscale modeling of drying as a powerful extension of the macroscopic approach: application to solid wood and biomass processing. Drying Technology 28, 944–959. doi:10.1080/07373937.2010.497079.

Perré, P., Almeida, G., Ayouz, M., Frank, X., 2015. New modelling approaches to predict wood properties from its cellular structure: image-based representation and meshless methods. Annals of Forest Science 73, 147–162. doi:10.1007/s13595-015-0519-0.

Perré, P., Turner, I., 2001. Determination of the material property variations across the growth ring of softwood for use in a heterogeneous drying model. part 2. use of homogenisation to predict bound liquid diffusivity and thermal conductivity. Holzforschung 55, 417–425. doi:10.1515/HF.2001.069.

Pierre, T., Colinart, T., Glouannec, P., 2014. Measurement of Thermal Properties of Biosourced Building Materials. Int J Thermophys 35, 1832–1852. doi:10.1007/s10765-013-1477-0.

Quenjel, E.H., Perré, P., 2022. Computation of the effective thermal conductivity from 3D real morphologies of wood. Heat and Mass Transfer 58, 2195–2206. doi:10.1007/s00231-022-03246-7.

Real, S., Bogas, J.A., Gomes, M.d.G., Ferrer, B., 2016. Thermal conductivity of structural lightweight aggregate concrete. Magazine of Concrete Research 68, 798–808. doi:10.1680/jmacr.15.00424.

Sáez-Pérez, M.P., Brümmer, M., Durán-Suárez, J.A., 2020. A review of the factors affecting the properties and performance of hemp aggregate concretes. Journal of Building Engineering 31, 101323. doi:10.1016/j.jobe.2020.101323.

Sanchez-Palencia, E., 1983. Homogenization method for the study of composite media, in: Asymptotic Analysis II. Springer, pp. 192–214.

Seng, B., Magniont, C., Lorente, S., 2019. Characterization of a precast hemp concrete block. Part II: Hygric properties. J. Building Engineering 24, 100579. doi:10.1016/j.jobe.2018.09.007.

Shea, A., Lawrence, M., Walker, P., 2012. Hygrothermal performance of an experimental hemp–lime building. Construction and Building Materials 36, 270–275. doi:10.1016/j.conbuildmat.2012.04.123.

Tran-Le, A.D., Nguyen, S.T., Langlet, T., 2019. A novel anisotropic analytical model for effective thermal conductivity tensor of dry lime-hemp concrete with preferred spatial distributions. Energy Buildings 182, 75–87. doi:10.1016/j.enbuild.2018.09.043.

UN environnement, 2016. Annual Report 2016, Empowering People to Protect the Planet. Technical Report.

Walker, R., Pavía, S., 2014. Moisture transfer and thermal properties of hemp–lime concretes. Construction and Building Materials 64, 270–276. doi:10.1016/j.conbuildmat.2014.04.081.

Walker, R., Pavia, S., Mitchell, R., 2014. Mechanical properties and durability of hemp-lime concretes. Construction and Building Materials 61, 340–348. doi:10.1016/j.conbuildmat.2014.02.065.

Wang, M., Pan, N., 2008. Predictions of effective physical properties of complex multiphase materials. Materials Science and Engineering: R: Reports 63, 1–30. doi:10.1016/j.mser.2008.07.001.

Williams, J., Lawrence, M., Walker, P., 2016. The influence of the casting process on the internal structure and physical properties of hemp-lime. Materials and Structures 50, 108. doi:10.1617/s11527-016-0976-4.

Williams, J., Lawrence, M., Walker, P., 2018. The influence of constituents on the properties of the bio-aggregate composite hemp-lime. Construction and Building Materials 159, 9–17. doi:10.1016/j.conbuildmat.2017.10.109.

Wulf, R., Mendes, M.A.A., Skibina, V., Al-Zoubi, A., Trimis, D., Ray, S., Gross, U., 2014. Experimental and numerical determination of effective thermal conductivity of open cell FeCrAl-alloy metal foams. Int. J. of Thermal Sciences 86, 95–103. doi:10.1016/j.ijthermalsci.2014.06.030.

Yu, Z.T., Xu, X., Fan, L.W., Hu, Y.C., Cen, K.F., 2011. Experimental Measurements of Thermal Conductivity of Wood Species in China: Effects of Density, Temperature, and Moisture Content. Forest Products Journal 61, 130–135. doi:10.13073/0015-7473-61.2.130.